Unexpected Observation of Disorder and Multiple Phase-Transition Pathways in Shock-Compressed Zr

Saransh Singh[1], Martin G. Gorman,[1] Patrick G. Heighway[2], Joel V. Bernier,[1] David McGonegle,[2,3] Hae Ja Lee,[4]
Bob Nagler,[4] Jon H. Eggert[1], and Raymond F. Smith[1]

[1]*Lawrence Livermore National Laboratory, Livermore, California, USA*
[2]*Department of Physics, Clarendon Laboratory, University of Oxford, Oxford, United Kingdom*
[3]*Oxford Centre for High Energy Density Science, Department of Physics, Clarendon Laboratory,*
University of Oxford, Oxford, United Kingdom
[4]*Linac Coherent Light Source, SLAC National Accelerator Laboratory, Menlo Park, California, USA*

The response of materials under dynamic compression involves a complex interplay of various deformation mechanisms aimed at relieving shear stresses, yielding a remarkable diversity in material behavior. In this Letter, we utilize femtosecond x-ray diffraction coupled with nanosecond laser compression to reveal an intricate competition between multiple shear-relieving mechanisms within an elemental metal. Our observations in shocked-compressed single-crystal Zr indicate a disorder-mediated shear relaxation at lower pressures. Above the phase-transition pressure, we observe the increasing contribution of structural phase transition in relieving shear stress. We detect not one but three concurrent pathways during the transition from the hcp to a hex-3 structure. These complex dynamics are partially corroborated through multimillion-atom molecular dynamics simulations employing a machine-learned interatomic potential. Our observation of multiple concurrent pathways and disorder during shock compression underscore the far greater intricacies in the dynamic response of metals than previously assumed.

There are several possible mechanisms by which materials relieve shear stress when subjected to uniaxial shock compression, such as dislocation generation and motion, twinning, stacking fault generation, shear-induced amorphization, and phase transformation. The interplay of these mechanisms produce a rich diversity in the response of materials subjected to dynamic compression. Metals respond predominantly via dislocation motion, twinning [1,2], and generation of stacking faults [3,4]. To our knowledge, no instances are known of elemental metals exhibiting disorder upon shock loading. Covalently bonded materials, on the other hand, most commonly exhibit shear-induced amorphization as an additional deformation mechanism [5]. The prevalence of dislocation activity is believed to influence the likelihood of forming amorphous bands during plastic loading. However, disorder as a deformation mechanism is impeded in metals due to the relatively facile activation of alternative deformation mechanisms.

Solid-solid structural phase transitions are also a shear-stress-relieving mechanism across all material classes and have also been an active area of investigation for the last hundred years [6–12]. Advancements in ultrabright sources like x-ray free-electron lasers (XFELs) have enabled *in situ* measurements within solids dynamically compressed to extraordinary, planetary-scale pressures over mere nanoseconds. Recent research efforts have increasingly focused on using diffraction not only to discover exotic high-pressure phases [13–15], but also to study the interplay of different deformation mechanisms such as slip and twinning [1], and to identify atomistic pathways during structural phase transitions induced by dynamic compression [4,16–18]. The conventional picture of atomistic pathways is based on atomic mapping from an ordered parent phase to an ordered daughter phase via a unique set of lattice strains and atomic shuffles. In Zr and many materials, differing atomistic modeling approaches present conflicting results. Each transition pathway is differentiated by the crystal orientation within the daughter phase relative to its parent. Thus, by measuring the orientation relationship (OR) between specific crystallographic planes and directions within the parent and daughter phases using diffraction, one can experimentally constrain the atomistic transition mechanism. Identifying these mechanisms provides the most stringent tests for our state-of-the-art theoretical and computational models.

Because of the commercial and technological importance of the hexagonally closed-packed (hcp) zirconium (Zr) and titanium (Ti), the high-pressure response of these metallic systems has been the subject of intense theoretical and experimental scrutiny. However, limited experimental measurement of the deformation mechanisms in Zr exists at very high-strain rates ($\sim 10^7$–10^8 s^{-1}). This is partly due to its noncubic nature, simultaneously activating competing slip and twinning systems [2]. Additionally, Zr undergoes a
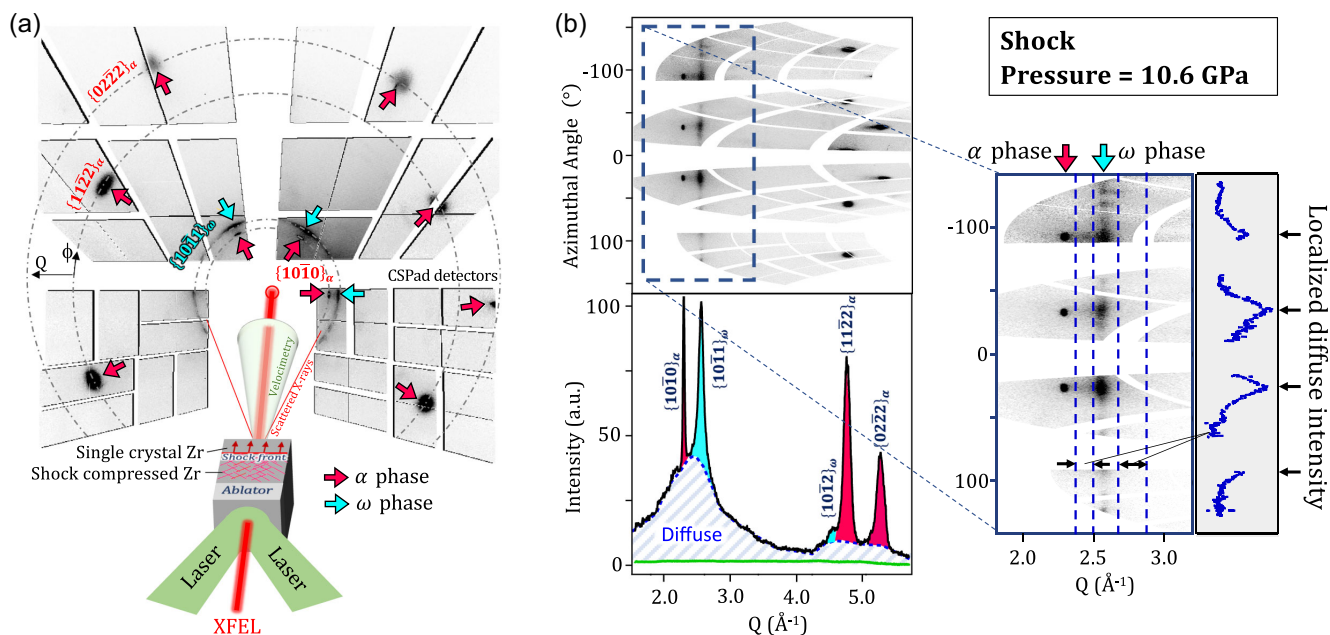
FIG. 1. Experimental setup for x-ray diffraction measurements of shock-compressed single-crystal Zr samples. (a) The 10-keV, 50-fs output of the LCLS-XFEL probed the shock-compressed Zr and produced an x-ray diffraction signal as recorded on CSPADs [19]. Here, the diffraction angle (2θ) and consequently $Q = 4\pi \sin\theta/\lambda$ increases radially, with azimuthal angle (ϕ) defined around the Debye-Scherrer cones. λ denotes the wavelength of the x rays. These data provide information on crystal structure, sample density, and microstructural texture, while velocimetry measurements provide information on shock timing and pressure uniformity during the x-ray probe period [20]. The diffraction data shown (10.6 GPa) are consistent with multiple reflections from the compressed α phase (red arrows) and a single reflection from the ω phase (cyan arrows). (b) We present the same diffraction data in Q-ϕ coordinates. The Debye-Scherrer rings appear as straight lines in this view. We show the ϕ-averaged lineout in the lower panel, where the green curve represents the detector background. The peaks from the α and ω phase are shaded with red and cyan colors, respectively. We reproduce an enlarged view of the lower diffraction-angle region in the inset. The lineout to the right of the inset shows the azimuthal variation of the diffuse signal between the Bragg peaks noted by the dashed vertical lines.

structural phase transition from the ductile hcp (α phase) to the brittle simple hexagonal (ω phase) at high pressures, compounding the challenges in data analysis. Additionally, there is no scientific consensus about the mechanism of the $\alpha \to \omega$ structural phase transition in Zr [21–39], which is an important shear-relieving mechanism in Zr. Existing literature suggests two distinct ORs during the $\alpha \to \omega$ phase transition. Most shock-compression studies on recovered samples have observed what we will call the variant I OR [27–29]. In contrast, the majority of static-compression and high-pressure torsion studies report variant II [21–23,32–34] (see Supplemental Material Table S1 [40]). Several studies, however, deviate from this trend for reasons that remain unclear [24–26]. As a result, a comprehensive understanding of high-strain rate deformation in Zr remains elusive.

We approach the $\alpha \to \omega$ phase transition from a new direction by combining uniaxial laser-shock compression of high-purity, well-oriented single-crystal Zr with *in situ* diffraction measurements using a high-brightness femtosecond XFEL source. The short probe duration produces near-instantaneous snapshots of atoms in the high-pressure shocked state as the material deforms. The single-crystal

nature of our samples aids in the data interpretation by producing textured diffraction data, which allow us to decouple the effects of various deformation mechanisms and provides a comprehensive picture of the Zr response across the $\alpha - \omega$ phase boundary.

Laser-driven shock-compression experiments were performed at the matter in extreme conditions (MEC) end station of the Linac Coherent Light Source (LCLS) [63,64]. Figure 1(a) shows a schematic of the experimental setup and target design used at MEC. The target consisted of a 50-μm-thick polyimide ablator and a 40-μm-thick Zr single crystal with the [0001] direction parallel to the sample normal (shock direction). The samples were oriented to within $< 1°$ of the [0001] axis. An impurity analysis confirmed $> 99.95\%$ purity and an ambient-pressure density of 6.52 g/cm^3. We focused the output of the 527-nm drive laser at MEC, temporally shaped into a 15-ns flattop pulse, into a 250-μm spot on the front of the polyimide. This generated an ablatively driven shock into the target assembly, which applied a uniaxial load along the c axis of the Zr crystal. Shock pressure in the sample is directly proportional to the laser intensity and, therefore, precise control of the on-target energy allowed for tuning of the
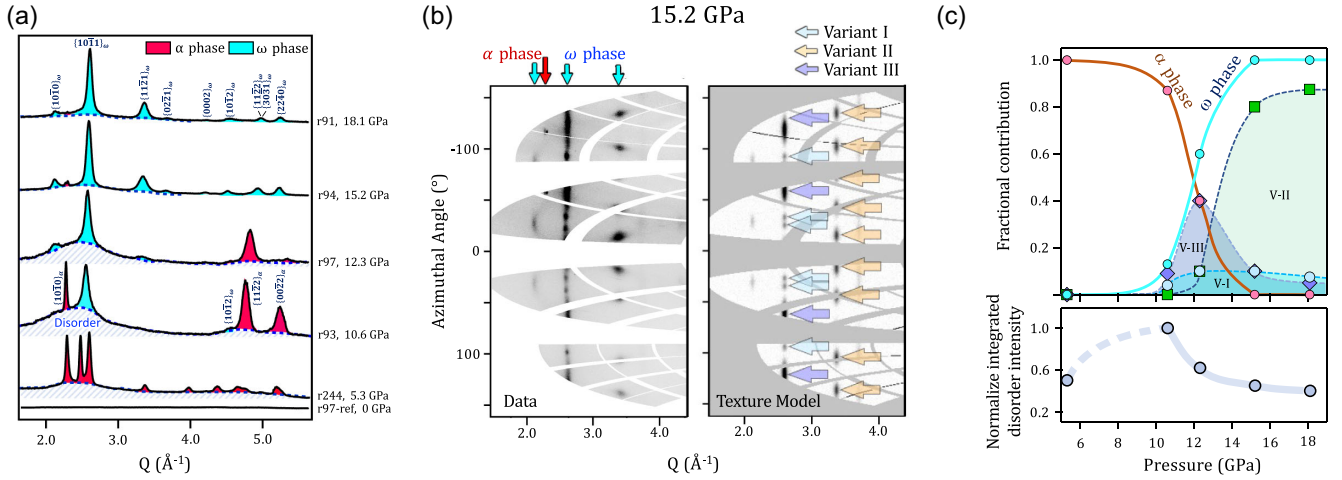
FIG. 2. Evolution of diffraction signal as a function of shock pressure. (a) Waterfall plot of azimuthally averaged lineouts from single-crystal Zr targets. The diffuse scattering signal peaks near the $\alpha \rightarrow \omega$ phase-transition pressure. We note that the sample used in run 244 had surface polishing features leading to more diffraction peaks from the α phase compared to the other samples. (b) Experimental and modeled diffraction patterns from shock-compressed single-crystal zirconium at 15.2 GPa. We modeled the crystallographic texture of the ω phase as the sum of unimodal distributions centered around the 12 orientations of the variant I OR, 3 orientations of variant II OR, and 6 orientations of the variant III OR. We show the region with diffraction from the $\{10\bar{1}0\}_\alpha$, $\{10\bar{1}1\}_\omega$, and $\{11\bar{2}1\}_\omega$ planes. Contributions to the $\{10\bar{1}1\}_\omega$ diffraction from the ORs of variants I and III are azimuthally separated and indicated by the cyan and blue arrows, respectively. Diffraction from the $\{11\bar{2}1\}_\omega$ plane originates entirely from variant II OR. (c) The volume fraction of each OR formed within the ω phase shows a strong pressure dependence. We observe the dominance of variant III OR at low pressures, which variant II OR eventually supplants at higher pressures. The integrated diffuse is normalized with respect to the integrated diffuse intensity of shot 93.

pressure within the Zr sample [64]. Eight targets were compressed with peak pressures ranging from 5.3 to 21.3 GPa. During shock transit, an ultrabright 50-fs 10-keV XFEL pulse, incident normal to the target, scattered off the compressed Zr and produced volume-integrated x-ray diffraction. The signal was recorded on the Cornell-Stanford pixel array detectors (CSPADs) in transmission geometry [19]. The x-ray probe time in our experiments was set to ensure the same shock-compressed Zr volume from shot to shot, as determined by the velocimetry measurements (see Supplemental Material Fig. S1 [40]).

Figure 1(a) shows the 2D orthographic view of diffraction data for a shock pressure of 10.6 GPa (marginally above the phase-transition pressure). While the Zr sample loses its simple single crystalline nature upon shock compression, it retains a highly oriented microstructure, as seen in the localized intensity around the Debye-Scherrer diffraction rings. At this pressure, we observe diffraction signals from the compressed α and ω phases. We do not measure any diffraction from the uncompressed material ahead of the shock front due to the highly oriented nature of the zirconium foil (see Supplemental Material Fig. S2 [40]). We also observe a diffuse background signal superimposed on top of sharp Bragg peaks. This diffuse signal [marked by dashed lines in the Fig. 1(b) inset] in the intervening regions between the Bragg peaks is observed to be nonuniform azimuthally and has an angular period of 60° indicating a sixfold symmetry. The azimuthally localized diffuse signal

reveals itself only in our single-crystal scattering configuration; we do not observe it in our polycrystalline Zr diffraction data (see Supplemental Material Fig. S3 [40] and accompanying text).

Figure 2(a) shows the azimuthally averaged lineouts at five pressures. The peaks originating from the α and ω phases are shaded in red and cyan, respectively. At 5.3 GPa, the diffraction signal is consistent with the presence of only the α phase. Surprisingly, we also observe a diffuse background signal. At 10.6 GPa, close to the phase-transition pressure, the Bragg diffraction signal is still dominated by the α phase with one single ω-phase peak. However, there is a rise in the diffuse scattering signal as compared to the lower-pressure shot. Upon further increase in pressure away from the phase-transition boundary, the strength of the Bragg diffraction signal from the α phase recedes in intensity. This is also accompanied by a reduction of the diffuse scattering signal. At 18.1 GPa, the diffraction is almost exclusively from the high-pressure ω phase with a tiny diffuse scattering background.

The azimuthal intensity distribution in the Debye-Scherrer rings encodes the orientation relationship between the α and ω phases. We extract this information by constructing a forward model to calculate the expected diffraction signal for our experimental geometry. This model accounts for x-ray beam energy and direction, detector positions, and crystallographic information about the sample, such as crystal structure, unit cell dimensions

on compression, phase volume fraction, and crystallographic texture of each phase (see Supplemental Material Sec. S4 [40] and Ref. [18] for further details). The results of the forward model calculation for the 15.2 GPa shot are presented in Fig. 2(b). We determined the phase fractions of the ω phases to be close to 100% for this shot. A unique phase-transition pathway proved inadequate in reproducing the experimentally observed azimuthal intensity distribution. Instead, we determined the diffraction data to be consistent with ω-phase orientations from three distinct phase-transition pathways: variants I, II, and III. For clarity, we only show the variant contributions to first two Debye-Scherrer rings. While variant I and II ORs have been previously reported in numerous studies, variant III OR has never been observed experimentally. We present the pressure dependence of the phase-fraction evolution, the relative abundance of the different variants within the ω phase, and the integrated diffuse background signal in Fig. 2(c). The phase fraction of the α phase decreases with increasing pressure as expected. In the ω-phase volume, we observe three competing phase-transition pathways vying for dominance. Variant III dominates at lower pressures and is eventually superseded by variant II as the pressure increases. We refer the readers to Supplemental Material Fig. S4 [40] for our semiquantitative method of determining the phase fractions of different phases and the relative abundance of the various variants and Supplemental Material Fig. S5 [40] for a comprehensive collection of the forward model results with increasing pressure. We considered basal or pyramidal stacking faults as the source of azimuthally modulated diffuse scattering signal. However, we did not find consistency of the observed diffraction signal with the signal generated by these configurations. We refer the readers to Supplemental Material Sec. S5 and Figs. S6 and S7 [40] for more details. To investigate the origin of the diffuse signal, we performed large-scale classical molecular dynamics (MD) simulations of [0001]-oriented Zr single crystals with initial dimensions of $40 \times 40 \times 100$ nm^3 shocked to 15 GPa using LAMMPS [66]. We modeled the interatomic interactions using the machine-learned potential of Zong *et al.* [39], which was tailored to model allotropy in Zr at pressures of up to 30 GPa. These simulations allow us to see in microscopic detail the dynamics unfolding in the wake of the shock and to analyze the structure factor of the complex atomistic configuration that results. We refer the readers to the companion article [67], Supplemental Material Sec. S6 [40] and references therein for further details about the molecular dynamics simulations.

Figure 3(a) shows a visualization of the computational cell 18 ps into the simulation, with atoms colored according to their local phase (above) and shear stress (below). The shock is led by an elastic precursor, behind which the pressure and shear stress are elevated to 10.0 and 3.5 GPa, respectively. However, the crystal retains a strained α-phase

structure. Trailing this precursor is a phase-transition front that raises the pressure to 15 GPa while relaxing the shear stress to 0.9 GPa, heralding the onset of the $\alpha \rightarrow \omega$ transition and the generation of disorder. Since the drop in shear stress is correlated to both the onset of the phase transition and the generation of disorder, we conclude that these are shear-relieving mechanisms in c-oriented Zr. The resulting clusters of disordered atoms form 10% of the cell by mass and occupy the interstices between the larger ω grains (which constitute 60%). Though noncrystalline, the atomistic structure of these nanoclusters shows orientational order and a structure factor qualitatively similar to that of the ω phase (see Supplemental Material Figs. S8 and S9 [40] for the radial and angular distribution functions and the structure factors of the ω and noncrystalline structures, respectively). We note that the orientational order in the disordered clusters makes it more accurate to refer to these atoms as partially disordered. We also note that identical shock simulations below the phase-transition boundary at 8 GPa did not generate disordered atoms, which is in disagreement with the observation of a diffuse background at 5.3 GPa as shown in Fig. 2(b). We will explore the reason for this disagreement in future experimental and computational studies.

In Fig. 3(b), we show synthetic diffraction generated by the phase-transformed region of the simulation cell with 10-keV x rays. Sharp diffraction peaks attributable to ω grains with the variant I and II OR are visible at Bragg angles similar to those measured in the experiment and at identical azimuthal angles. The difference in peak intensities is due to the strong sensitivity of the Bragg condition to the ω phase's c/a ratio, which at 15 GPa takes values of 0.605 and 0.621 in the experiment and simulation, respectively. In addition to these Bragg peaks, we observe a diffuse diffraction signal centered at 29° akin to that seen in the data. Like the experimental signal, this diffuse diffraction is anisotropic and exhibits the same sixfold modulations around the Debye-Scherrer ring. The missing $\{0001\}_\omega$ and $\{10\bar{1}1\}_\omega$ peaks in the simulated diffraction signal are due to the absence of variant I and III ORs in the simulation.

In our MD simulations, the majority ($\sim$95%) of the ω phase assumes the variant II OR, with a small fraction ($\sim$5%) of variant I OR present. While there is qualitative agreement of the simulations with the experiment, the quantitative phase fractions do not agree. In addition, variant III OR is completely absent from our simulations. The simulation properties can rationalize this behavior. We posit that variant I is made rare by the artificially high shear-stress environment created in these idealistic simulations in perfect, defect-free crystals. In the presence of defects, some plasticity before the phase transition will bring about the low shear-stress environment that favors variant I OR over variant II. We will explore this hypothesis further in a planned future manuscript. We believe the
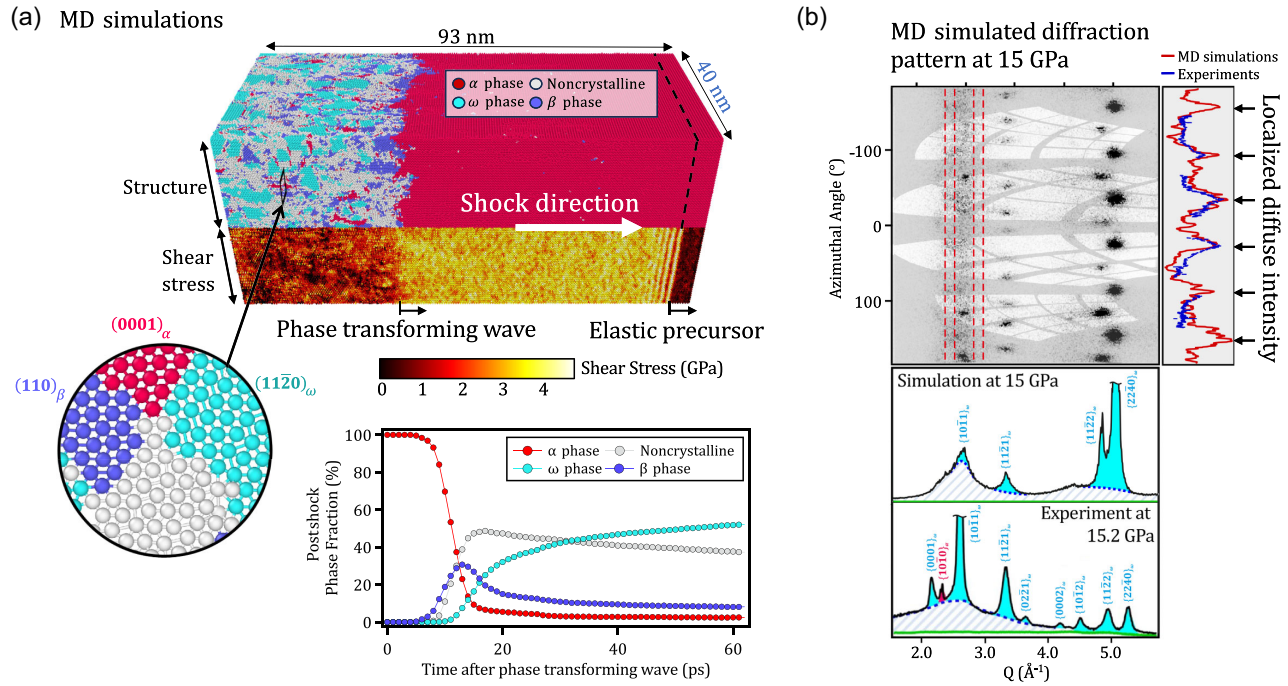
FIG. 3. Molecular dynamic simulations with machine-learning potential. (a) Visualization of a Zr single crystal with initial dimensions of $40 \times 40 \times 100$ nm³ shock-compressed along [0001] to 15 GPa, with atoms colored according to their local phase (above) and shear stress (below) after 18 ps, performed using OVITO [65]. Below is the time evolution of the α, β, ω, and noncrystalline phase fractions (the last group includes partially disordered nanoclusters and atoms on grain boundaries). The circular inset shows the local arrangement of atoms in a region of phase coexistence, viewed in a plane normal to the shock. (b) Synthetic diffraction generated 200 ps into the simulation using 10-keV x rays. Top: the full diffraction pattern in polar coordinates, with a semitransparent mask added to simulate gaps in the CSPADs. Lower: compares azimuthally averaged lineouts from the simulation (15 GPa) and experiment (15.2 GPa). Right: the azimuthal variation of the simulated diffuse signal centered at $2\theta \sim 30°$, with averages taken over the windowed region (red-boxed region). We overlay the azimuthal distribution of the azimuthally localized diffuse signal from the experimental data (shot 93) in blue.

absence of variant III in our simulations results from the interatomic potential's inability to model the energy landscape of Zr accurately along the variant III pathway. As this transformation pathway was unknown, its configuration space was not used in training the potential. Exploration of this new pathway via first-principles atomistic simulations is warranted.

The new variant III OR we observe in our experiments has never been observed in quenched ω-Zr captured from recovery experiments. This observation is in contrast to numerous experimental static and dynamic-compression studies reporting variant I and variant II ORs [21–25,27–29,32–34]. In a recovery study of shock and pressure released Zr, samples that completely transformed to the ω phase during shock loading retained between 0% and 48% of the high-pressure phase in recovered samples [68]. The lack of any experimental observation of the variant III OR in recovered samples could be related to an OR dependence of the $\omega \rightarrow \alpha$ reverse phase transition. Upon pressure release, we hypothesize a complete reversion of the variant III ω-phase orientations to the α phase, but hysteresis for the other variants.

Our MD simulations predict a small amount of the intermediate bcc β phase in the tens of picoseconds

timescale. Our forward diffraction model predicts that the $\{220\}_\beta$ reflection should be observable in our experiments for the expected Burgers OR [11] between the hcp α phase and the bcc β phase. Although not conclusive, our diffraction data hint at the presence of this intermediate bcc phase. We refer the readers to Supplemental Material Figs. S10 and S11 [40] and accompanying text for more details.

In summary, we have demonstrated for the first time that the dynamic behavior of the elemental metal Zr under shock compression is far more intricate than previously thought, involving multiple competing phase-transition pathways and a partially disordered state as a shear-stress-relieving mechanism in a single nanosecond shock volume. While we initially attempted to use the more conventional embedded atom model potential for Zr, only the machine-learned interatomic potential partially reproduced our experimental observations. Our experiments and analysis highlight the importance of *in situ* measurements on highly oriented crystals in validating our best theoretical models at extreme conditions. While our results focus on zirconium, we expect our results to apply to the transformation dynamics of other material systems at high pressure and temperature.

[1] C. E. Wehrenberg, D. McGonegle, C. Bolme, A. Higginbotham, A. Lazicki, H. J. Lee, B. Nagler, H.-S. Park, B. A. Remington, R. E. Rudd, M. Sliwa, M. Suggit, D. Swift, F. Tavella, L. Zepeda-Ruiz, and J. S. Wark, Nature (London) **550**, 496 (2017).

[2] S. J. Turneaure, P. Renganathan, J. M. Winey, and Y. M. Gupta, Phys. Rev. Lett. **120**, 265503 (2018).

[3] S. M. Sharma, S. J. Turneaure, J. M. Winey, P. A. Rigg, N. Sinclair, X. Wang, Y. Toyoda, and Y. M. Gupta, Phys. Rev. X **10**, 011010 (2020).

[4] M. Sims, R. Briggs, T. J. Volz, S. Singh, S. Hamel, A. L. Coleman, F. Coppari, D. J. Erskine, M. G. Gorman, B. Sadigh, J. Belof, J. H. Eggert, R. F. Smith, and J. K. Wicks, J. Appl. Phys. **132** (2022).

[5] S. Zhao, B. Li, B. Remington, C. Wehrenberg, H. Park, E. Hahn, and M. Meyers, Mater. Today **49**, 59 (2021).

[6] P. W. Bridgman, Proc. Am. Acad. Arts Sci. **47**, 441 (1912).

[7] E. Bain, Trans. Am. Inst. Min., Metall. Pet. Eng. **70**, 25 (1924), https://hdl.handle.net/2027/uc1.b3219027.

[8] G. Kurdjumow and G. Sachs, Z. Phys. **64**, 325 (1930).

[9] H. Shöji, Z. Kristallogr. Cryst. Mater. **77**, 381 (1931).

[10] G. Wassermann, Arch. Eisenhüttenwes. **6**, 347 (1933).

[11] W. Burgers, Physica (Amsterdam) **1**, 561 (1934).

[12] Z. Nishiyama, Sci. Rep. Tóhoku Imp. Univ. **23**, 637 (1934), https://cir.nii.ac.jp/crid/1570854175128630400.

[13] P. D. Asimow, C. Lin, L. Bindi, C. Ma, O. Tschauner, L. S. Hollister, and P. J. Steinhardt, Proc. Natl. Acad. Sci. U.S.A. **113**, 7077 (2016).

[14] A. L. Coleman, M. G. Gorman, R. Briggs, R. S. McWilliams, D. McGonegle, C. A. Bolme, A. E. Gleason, D. E. Fratanduono, R. E. Smith, E. Galtier *et al.*, Phys. Rev. Lett. **122**, 255704 (2019).

[15] D. N. Polsin, A. Lazicki, X. Gong, S. J. Burns, F. Coppari, L. E. Hansen, B. J. Henderson, M. F. Huff, M. I. McMahon, M. Millot, R. Paul, R. F. Smith, J. H. Eggert, G. W. Collins, and J. R. Rygg, Nat. Commun. **13**, 2534 (2022).

[16] J. Hawreliak, J. D. Colvin, J. H. Eggert, D. H. Kalantar, H. E. Lorenzana, J. S. Stölken, H. M. Davies, T. C. Germann, B. L. Holian, K. Kadau, P. S. Lomdahl, A. Higginbotham, K. Rosolankova, J. Sheppard, and J. S. Wark, Phys. Rev. B **74**, 184107 (2006).

[17] S. Pandolfi, S. B. Brown, P. G. Stubley, A. Higginbotham, C. A. Bolme, H. J. Lee, B. Nagler, E. Galtier, R. L. Sandberg, W. Yang, W. L. Mao, J. S. Wark, and A. E. Gleason, Nat. Commun. **13**, 5535 (2022).

[18] S. Singh, R. Briggs, M. G. Gorman, L. X. Benedict, C. J. Wu, S. Hamel, A. L. Coleman, F. Coppari, A. Fernandez-Pañella, C. McGuire, M. Sims, J. K. Wicks, J. H. Eggert, D. E. Fratanduono, and R. F. Smith, Phys. Rev. B **108**, 184104 (2023).

[19] S. Herrmann, S. Boutet, B. Duda, D. Fritz, G. Haller, P. Hart, R. Herbst, C. Kenney, H. Lemke, M. Messerschmidt, J. Pines, A. Robert, M. Sikorski, and G. Williams, Nucl. Instrum. Methods Phys. Res., Sect. A **718**, 550 (2013).

[20] P. M. Celliers, D. K. Bradley, G. W. Collins, D. G. Hicks, T. R. Boehly, and W. J. Armstrong, Rev. Sci. Instrum. **75**, 4916 (2004).

[21] J. Silcock, Acta Metall. **6**, 481 (1958).

[22] G. Sargent and H. Conrad, Mater. Sci. Eng. **7**, 220 (1971).

[23] A. Rabinkin, M. Talianker, and O. Botstein, Acta Metall. **29**, 691 (1981).

[24] M. P. Usikov and V. A. Zilbershtein, Phys. Status Solidi (a) **19**, 53 (1973).

[25] A. R. Kutsar, I. V. Lyasotski, A. M. Podurets, and A. F. Sanches-bolinches, High Press. Res. **4**, 475 (1990).

[26] T. D. Swinburne, M. G. Glavicic, K. M. Rahman, N. G. Jones, J. Coakley, D. E. Eakins, T. G. White, V. Tong, D. Milathianaki, G. J. Williams, D. Rugg, A. P. Sutton, and D. Dye, Phys. Rev. B **93**, 144119 (2016).

[27] S. G. Song and G. T. G. III, Philos. Mag. A **71**, 275 (1995).

[28] G. Jyoti, K. Joshi, S. C. Gupta, and S. Sikka, Philos. Mag. Lett. **75**, 291 (1997).

[29] G. Jyoti, R. Tewari, K. Joshi, D. Srivastava, G. Dey, S. Gupta, S. Sikka, and S. Banerjee, in *Phase Transformation and Diffusion*, Defect and Diffusion Forum (Trans Tech Publications Ltd., Stäfa-Zurich, Switzerland, 2008), Vol. 279, pp. 133–138.

[30] D. R. Trinkle, A theoretical study of the HCP to omega martensitic phase transition in titanium, Ph.D. thesis, The Ohio State University, 2003.

[31] D. R. Trinkle, R. G. Hennig, S. G. Srinivasan, D. M. Hatch, M. D. Jones, H. T. Stokes, R. C. Albers, and J. W. Wilkins, Phys. Rev. Lett. **91**, 025701 (2003).

[32] H.-R. Wenk, P. Kaercher, W. Kanitpanyacharoen, E. Zepeda-Alarcon, and Y. Wang, Phys. Rev. Lett. **111**, 195701 (2013).

[33] N. Adachi, Y. Todaka, H. Suzuki, and M. Umemoto, Scr. Mater. **98**, 1 (2015).

[34] H. Wang, W. Dmowski, Z. Wang, J. Qiang, K. Tsuchiya, Y. Yokoyama, H. Bei, and T. Egami, Appl. Phys. Lett. **114**, 061903 (2019).

[35] H. Zong, T. Lookman, X. Ding, S.-N. Luo, and J. Sun, Acta Mater. **65**, 10 (2014).

[36] H. Zong, T. Lookman, X. Ding, C. Nisoli, D. Brown, S. R. Niezgoda, and S. Jun, Acta Mater. **77,** 191 (2014).

[37] S.-H. Guan and Z.-P. Liu, Phys. Chem. Chem. Phys. **18,** 4527 (2016).

[38] S. Rawat and N. Mitra, Comput. Mater. Sci. **126,** 228 (2017).

[39] H. Zong, Y. Luo, X. Ding, T. Lookman, and G. J. Ackland, Acta Mater. **162,** 126 (2019).

[40] See Supplemental Material at http://link.aps.org/supplemental/10.1103/PhysRevLett.133.096101 for a complete set of experimental data collected and analysis techniques used in this Letter, which includes Refs. [41–62].

[41] W. Pitsch and A. Schrader, Arch. Eisenhüttenwes. **29,** 715 (1958).

[42] H. Mao, W. A. Bassett, and T. Takahashi, J. Appl. Phys. **38,** 272 (1967).

[43] J. Gjønnes and T. Östmoe, Int. J. Mat. Res. **61,** 604 (1970).

[44] D. Potter, J. Less Common Metals **31,** 299 (1973).

[45] A. Crawley and K. Milliken, Acta Metall. **22,** 557 (1974).

[46] W. Rong and G. Dunlop, Acta Metall. **32,** 1591 (1984).

[47] S. G. Song, H. Du, and E. Y. Sun, Metall. Mater. Trans. A **33,** 1963 (2002).

[48] L. Al'Tshuler, A. Bakanova, I. Dudoladov, E. Dynin, R. Trunin, and B. Chekin, J. Appl. Mech. Tech. Phys. **22,** 145 (1981).

[49] J. M. Walsh, M. H. Rice, R. G. McQueen, and F. L. Yarger, Phys. Rev. **108,** 196 (1957).

[50] R. McQueen, S. Marsh, J. Taylor, J. Fritz, and W. Carter, High Velocity Impact Phenom. **293,** 294 (1970).

[51] P. Rigg, R. Saavedra, and R. Scharff, J. Phys. Conf. Ser. **500,** 032014 (2014).

[52] G. Caglioti, A. Paoletti, and F. Ricci, Nucl. Instrum. **3,** 223 (1958).

[53] P. Thompson, D. E. Cox, and J. B. Hastings, J. Appl. Crystallogr. **20,** 79 (1987).

[54] A. Kumar and P. R. Dawson, Comput. Methods Appl. Mech. Eng. **153,** 259 (1998).

[55] N. R. Barton, D. E. Boyce, and P. R. Dawson, Textures Microstruct. **35,** 372532 (2002).

[56] B. Warren, *X-Ray Diffraction*, Addison-Wesley Series in Metallurgy and Materials Engineering (Dover Publications, New York, 1990).

[57] S. M. Sharma, S. J. Turneaure, J. M. Winey, and Y. M. Gupta, Phys. Rev. B **102,** 020103(R) (2020).

[58] B. Yin, Z. Wu, and W. Curtin, Acta Mater. **123,** 223 (2017).

[59] H. Zong, P. He, X. Ding, and G. J. Ackland, Phys. Rev. B **101,** 144105 (2020).

[60] G. J. Ackland and A. P. Jones, Phys. Rev. B **73,** 054104 (2006).

[61] M. R. Armstrong *et al.*, JOM **73,** 2185 (2021).

[62] C. Cayron, J. Appl. Crystallogr. **40,** 1179 (2007).

[63] B. Nagler *et al.*, J. Synchrotron Radiat. **22,** 520 (2015).

[64] S. B. Brown, A. Hashim, A. Gleason, E. Galtier, I. Nam, Z. Xing, A. Fry, A. MacKinnon, B. Nagler, E. Granados *et al.*, Rev. Sci. Instrum. **88,** 105113 (2017).

[65] A. Stukowski, Model. Simul. Mater. Sci. Eng. **18,** 015012 (2010).

[66] A. P. Thompson, H. M. Aktulga, R. Berger, D. S. Bolintineanu, W. M. Brown, P. S. Crozier, P. J. in 't Veld, A. Kohlmeyer, S. G. Moore, T. D. Nguyen, R. Shan, M. J. Stevens, J. Tranchida, C. Trott, and S. J. Plimpton, Comput. Phys. Commun. **271,** 108171 (2022).

[67] P. G. Heighway, S. Singh, M. G. Gorman, D. McGonegle, J. H. Eggert, and R. F. Smith, companion paper, Phys. Rev. B **110,** 054113 (2024).

[68] M. G. Gorman, D. McGonegle, S. J. Tracy, S. M. Clarke, C. A. Bolme, A. E. Gleason, S. J. Ali, S. W. Hok, C. Greeff, P. G. Heighway *et al.*, Phys. Rev. B **102,** 024101 (2020).